

# Differential Absorption Lidar to Measure Subhourly Variation of Tropospheric Ozone Profiles

Shi Kuang, John F. Burris, M. J. Newchurch, Steve Johnson, and Stephanie Long

**Abstract**—A tropospheric ozone Differential Absorption Lidar system, developed jointly by The University of Alabama in Huntsville and the National Aeronautics and Space Administration, is making regular observations of ozone vertical distributions between 1 and 8 km with two receivers under both daytime and nighttime conditions using lasers at 285 and 291 nm. This paper describes the lidar system and analysis technique with some measurement examples. An iterative aerosol correction procedure reduces the retrieval error arising from differential aerosol backscatter in the lower troposphere. Lidar observations with coincident ozonesonde flights demonstrate that the retrieval accuracy ranges from better than 10% below 4 km to better than 20% below 8 km with 750-m vertical resolution and 10-min temporal integration.

**Index Terms**—Differential Absorption Lidar (DIAL), lidar, ozone, remote sensing, troposphere.

## I. INTRODUCTION

**O**ZONE is a key trace-gas species within the troposphere. On the one hand, ozone is a precursor of the hydroxyl radical [1, pp. 199–200], which reacts with most trace species in the atmosphere. On the other hand, ozone is also a strong greenhouse gas influencing the climate by its radiative forcing [2]. *In situ* photochemistry and dynamic processes largely govern the distribution of tropospheric ozone [3]. Measuring ozone variability at high spatial and temporal resolution increases our understanding of tropospheric chemistry [4], [5], planetary boundary layer (PBL)–free-tropospheric exchange [6], [7], stratosphere–troposphere exchange [8]–[10], and the impact of lightning-generated  $\text{NO}_x$  on tropospheric ozone [11]–[14].

Several techniques currently exist for making range-resolved measurements of tropospheric ozone. The most common technique is the balloonborne electrochemical concentration cell,

which has monitored ozone since the 1960s. The ozonesonde profiles ozone with a 100-m vertical resolution from the surface to 35-km altitude with the accuracy of 5%–10% [15], [16]. Ozonesondes are attractive because of their low up-front cost and well-characterized behavior. However, they are not suitable for making continuous measurements because of logistical considerations. Interesting atmospheric phenomena that vary over periods less than one day are particularly difficult to monitor using balloon ozonesondes. Satellite observations can derive total column ozone [17] and stratospheric ozone [18]–[22] and extend measurements to altitudes that are inaccessible to ozonesondes. More recently, high-quality satellite observations of tropospheric ozone are becoming available [18], [23]–[33]. Although the satellite measurements can produce global maps of ozone, their current measurement uncertainties, along with their coarse spatial and temporal resolution, limit their ability to observe short-term variations in ozone. Lidars can supplement these techniques when a requirement exists for ozone retrievals with higher temporal (from 1 min to several hours) and vertical resolution (from tens of meters to 2 km). For example, lidars of the Network for the Detection of Atmospheric Composition Change [34], [35] are providing long-term observations of ozone, as well as aerosol, temperature, and water vapor. Although the up-front costs are considerably higher than for a balloon ozonesonde operation, lidars can acquire profiles continuously under both daytime and nighttime conditions. The spatial and temporal resolution of a lidar is more than sufficient to characterize short-term ozone variations for the photochemical studies of vertical processes.

Differential Absorption Lidar (DIAL) has been successfully used to measure ozone within the PBL [36], [37], the free troposphere [38]–[44], and the stratosphere [45]–[48] for several decades. DIAL is evolving from ground-based and airborne systems to systems that are suitable for long-term deployment in space [49]. The technique derives ozone concentrations by analyzing how rapidly the backscattered signals at two separate but closely spaced wavelengths, one strongly absorbed by ozone and the other less strongly absorbed, diminish with altitude. This measurement does not require knowledge of the absolute signal intensities but, rather, only the relative change of the two signals with respect to altitude. Using electronically gated detection permits range-resolved measurements to a resolution as small as several meters over acquisition times of several minutes. The ozone DIAL discussed in this paper is located in the southeastern U.S. and thus provides a unique observational site within an interesting scientific area [50] to study trace-gas transport at the midlatitudes for both the polluted PBL and the free troposphere.

Manuscript received July 31, 2009; revised March 9, 2010; accepted May 31, 2010. Date of publication November 15, 2010; date of current version December 27, 2010. This work was supported in part by the National Aeronautics and Space Administration's Science Mission Directorate and in part by the National Oceanic and Atmospheric Administration's National Environmental Satellite, Data, and Information Service.

S. Kuang and M. J. Newchurch are with the Atmospheric Science Department, The University of Alabama in Huntsville, Huntsville, AL 35805 USA (e-mail: mike@nssstc.uah.edu).

J. F. Burris is with the NASA Goddard Space Flight Center, Greenbelt, MD 20771 USA.

S. Johnson is with the NASA Marshall Space Flight Center, Huntsville, AL 35812 USA.

S. Long is with the Earth System Science Center, Huntsville, AL 35805 USA.

Color versions of one or more of the figures in this paper are available online at <http://ieeexplore.ieee.org>.

Digital Object Identifier 10.1109/TGRS.2010.2054834

TABLE I  
CHARACTERISTICS OF THE RAPCD OZONE DIAL SYSTEM

System	Specification	
Transmitter		
Pump lasers	Nd:YAG, 20 Hz repetition rate, 5-7 ns pulse length, 300 mJ pulse <sup>-1</sup> at 1064 nm, 50 mJ pulse <sup>-1</sup> at 532 nm	
Dye	Rhodamine 590 and 610	
Emitted UV	4 mJ pulse <sup>-1</sup> at 285 nm, divergence<1 mrad 3 mJ pulse <sup>-1</sup> at 291 nm, divergence<1 mrad	
Tuning range	277 to 303 nm for the final UV output	
Receiver	High-altitude channel	Low-altitude channel
Telescope	Newtonian, 40-cm diameter, f/4.5, 1.5-mrad FOV	Welch Mechanical Designs Cassegrain, 10-cm diameter, f/2.3, 4.3-mrad FOV
Band-pass filter	Center wavelength at 286.4 nm with a 11-nm FWHM. Transmittance is 35% at 285 nm and 20% at 291 nm	
Detector	Electron Tubes 9813QA, about 28% quantum efficiency	Hamamatsu R7400U-03, about 20% quantum efficiency
Signal processing	LICEL Transient Recorder (TR40-80), 250-MHz maximum photoncounting rate, 12-bit and 40-MHz analog-to-digital converter, 25-ns range resolution	

## II. SYSTEM DESCRIPTION

Housed in the Regional Atmospheric Profiling Center for Discovery (RAPCD), the tropospheric ozone DIAL system is located at 34.7250° N, 86.6450° W on the campus of The University of Alabama in Huntsville (UAHuntsville) within the Huntsville city limits at an elevation of 206 m above sea level. It is designed for measurements within the PBL and the free troposphere during both daytime and nighttime. Because of UAHuntsville's location and occasional high temperature and humidity conditions, heavy aerosol pollution is sometimes present. Compared with the clean free troposphere, these aerosols require a larger dynamic range for the detection system because of their larger optical depth. Moreover, the rapid change of aerosol concentrations (e.g., due to convective activity) increases the measurement uncertainty for DIAL within the PBL and lower troposphere. Judicious system-design choices and an effective aerosol correction scheme allow this system to produce high-quality ozone profiles under a variety of conditions.

### A. Wavelength Selection

The selection of the 285- and 291-nm wavelengths results from the balance of the following three considerations: 1) optimizing the altitude range to make retrievals; 2) reducing the impact of the solar background during daytime operation; and 3) reducing the impact of aerosol interference upon the ozone retrieval. The DIAL wavelength selection is flexible and optimized for the local ozone distribution, the absorption arising from non-ozone species, the measurement range, and

the specific system configuration, including the output power, the telescope mirror size, and the photomultiplier's (PMT's) dynamic range. Numerous publications (e.g., [51]) discussed the optimum wavelengths for tropospheric systems. Although shorter wavelengths can provide higher measurement sensitivity arising from the larger ozone differential cross section, they limit the maximum measurable range due to stronger attenuation of ozone absorption and Rayleigh (molecular) extinction and thus require more signal acquisition time. In addition, the shorter wavelengths require more dynamic range of the detection system and might require more altitude channels. With the current transmitter power, the online wavelength of 285 nm allows us to measure ozone up to 9 km under a clear sky and 7 km under aerosol loading with a 10-min temporal resolution. Because of the significant solar background during daytime operations, we choose 291 nm as the offline wavelength. Longer wavelengths will cause a significant increase in the solar background and reduce the signal-to-background ratio. To measure both wavelength channels using the same PMT and simplify the system design, we used a bandpass filter with a central wavelength of 286.4 nm and a full width at half maximum of 11 nm whose transmittance is  $\leq 10^{-8}$  at wavelengths longer than 300 nm. For a bandpass filter, the integrated sky background over the filter bandwidth and the dark counts actually determine the background for both offline and online wavelengths. For our lidar configuration, the 285- and 291-nm wavelength region can provide sufficient signal-to-background ratios at 8 km under most sky conditions. The retrieval errors due to aerosol interference are a concern in the PBL and lower troposphere. These errors are not a simple function of the wavelength separations because reducing the separation to

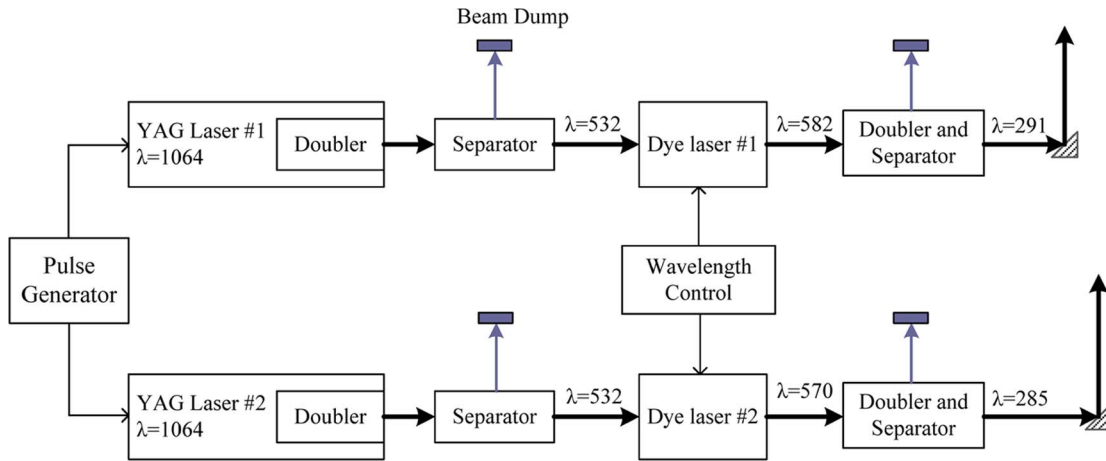


Fig. 1. Transmitter diagram.

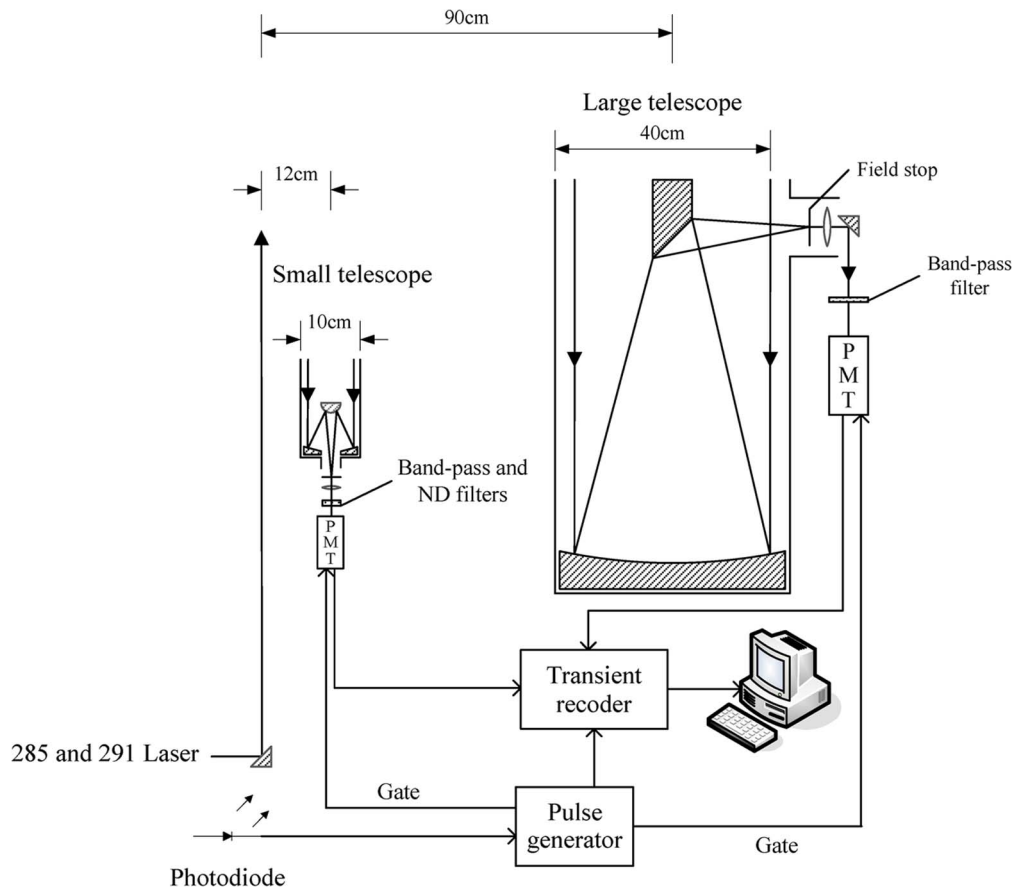


Fig. 2. Diagram of the receivers and detectors.

reduce the aerosol differential backscattering will also decrease the differential ozone cross section. These errors are sensitive to the local aerosol composition, size distribution, and vertical profile. Although the aerosol interference can be lower when our online wavelength extends to the steepest part of the ozone absorption cross section, this will significantly sacrifice the maximum measurable range. Therefore, the 285–291-nm pair is the optimal choice to balance the maximum measurable altitude, the impact of aerosol differential backscattering, and the impact of solar background.

*B. Hardware Components*

Table I lists the characteristics of the RAPCD ozone DIAL system. The transmitter consists of two identical dye lasers pumped by two separate frequency-doubled Nd:YAG lasers (Fig. 1). A pulse generator triggers each laser pulse with a 25-ms separation between the alternate pulses. The dye lasers are software controlled to select the user-defined wavelength. The knife-edge method [52] determines that the divergences of both UV laser beams are less than 1 mrad. A 0.75-m triple-grating monochromator (Acton Research

Corporation) indicates that the actual wavelengths of the outgoing UV lasers are 285 and 291 nm within an uncertainty of 0.1 nm.

The receiving system currently operates with two separate telescopes, as shown in Fig. 2. The high-altitude receiver uses a 40-cm Newtonian telescope, and the low-altitude channel employs a 10-cm Cassegrain telescope. The large telescope system routinely makes measurements from 3 to 8 km and, on occasion, measures ozone at 12 km. Employing a 1.5-mrad field of view (FOV), the large telescope achieves full overlap between the laser and receiver at about 3 km. Larger FOVs lower the altitude at which full overlap occurs but significantly increase solar background. The small telescope system currently retrieves ozone between 1 and about 5 km with a typical FOV of 4.3 mrad. The future plan is to extend the retrievals down to about 200 m with an additional altitude channel in the small telescope. The bandpass filters used to restrict the solar background for both receivers have a transmittance of 35% at 285 nm and 20% at 291 nm.

The detection system of the RAPCD ozone DIAL uses both photon counting (PC) and analog detection to facilitate operations over both altitude channels. This detection combination provides the linearity of the analog signal in the strong-signal region and high sensitivity of the PC signal in the weak-signal region. An EMI 9813 QA PMT, which has been used extensively for many years on a number of Goddard Space Flight Center lidar systems [53], [54], is used in the high-altitude channel, while a small Hamamatsu 7400 PMT is used in the low-altitude channel. A photodiode detects the outgoing laser pulses, which trigger both the PMT gating circuits and the Licel transient recorder (TR) (TR40-80, Licel Company, Germany). The Licel TR offers the advantage of increased dynamic range by providing simultaneous measurements using both analog detection and PC. The Licel TR's highest temporal resolution is 25 ns, corresponding to a fundamental range resolution of 3.75 m. It is necessary to gate the high-altitude channel off for the first 10–15  $\mu$ s and the low-altitude channel for the first 1  $\mu$ s to maintain the PMT's linearity and minimize the impact of signal-induced bias (SIB) on the background count rate.

### III. DATA PROCESSING

#### A. Raw Data Processing

Several operations, designed to improve the measurement precision, occur before the ozone retrieval. First, average the signal returns over 10 min and 150 m. The temporal resolution of the retrieval can be varied depending on the signal-to-noise ratio (SNR). Second, apply a dead-time correction to the PC signals. For PC at high counting rates, a second pulse arriving at the discriminator before it has recovered from the previous pulse will not be counted—a period known as dead time [55]. Experiments with a function-generator-driven LED determine this time to be 10 ns for the high-altitude channel and 4 ns for the low-altitude channel. Our results show that the system dead time obeys a nonparalyzable model following a simple relationship, as in [56, eq. (1)], between the true count rate  $C_T$

and measured count rates  $C_M$ , allowing the impact of dead time  $T_d$  on the data to be removed

$$C_T = \frac{C_M}{1 - C_M T_d}. \quad (1)$$

Third, remove the signal background. The last 10  $\mu$ s (400 fundamental bins) of signals ranging up to 30.72 km (far-range limit), which are considered to be the background region where no laser signal returns are expected, are averaged to give an approximate background. Fourth, merge the parallel analog and PC signals into a single profile [57] after removing the offset between the analog and PC signals [58]. We found this offset to be about 250 ns for our system by carefully comparing returns derived with clouds on both the analog and PC channels. The merged region requires that the ratio of PC to analog signals is constant. Ratios that are not constant suggest either an incorrect background subtraction or a wrong dead-time correction. The merging threshold of the PC signal is typically 20 MHz for the Hamamatsu PMT employed in our low-altitude channel and 20–30 MHz for the EMI PMT used on the high-altitude channel. Because DIAL retrievals depend on the quality of both 285- and 291-nm signals, we combine the PC and analog signals approximately at the same altitude for both lasers to minimize the retrieval error due to the merging. Examples of the ratio of PC to analog signals and their merged region for the 285-nm signal are shown in Fig. 3. The merging threshold is 20 MHz for both altitude channels. The fifth step involves smoothing the signals to reduce random noise. Our configuration currently employs a five-point ( $5 \times 150 = 750$  m) running average applied to returns from all altitudes; smoothing reduces the effective vertical resolution to 750 m.

After initial processing, an exponential-fit correction removes SIB from the signal returns. This bias, caused by intense light returns from the near range (also called signal-induced noise), appears as a slowly decaying noise source superimposed on the normal returns. The causes of the SIB are related to the regenerative effects such as dynode glow, after-pulsing effect, glass-charging effect, shielding effect, and helium penetration [59]. SIB varies widely with different PMTs. For our case, the SIB of the EMI 9813 is larger than that for the Hamamatsu 7400. SIB can persist for several hundreds of microseconds and can exert a strong influence on data at the lidar's upper range where both signal and noise counts become comparable. With uncorrected SIB, the raw signal falls off more slowly at higher altitudes, resulting in lower retrieved ozone values. SIB usually has more influence on the shorter wavelength channel, which falls off more rapidly with altitude. Unless a mechanical shutter physically blocks the optical path to the PMT to eliminate SIB, a model must characterize its behavior. Cairo *et al.* [60] and Zhao [61] have successfully used a double-exponential function for this purpose. However, this correction increases measurement uncertainties because both the scaling and exponential lifetimes are difficult to determine without additional independent measurements. A more practical technique is to employ a single-exponential fit to the residual background [42], [43], [62]. For the high-altitude channel, the function's coefficients are automatically determined using a single-exponential least

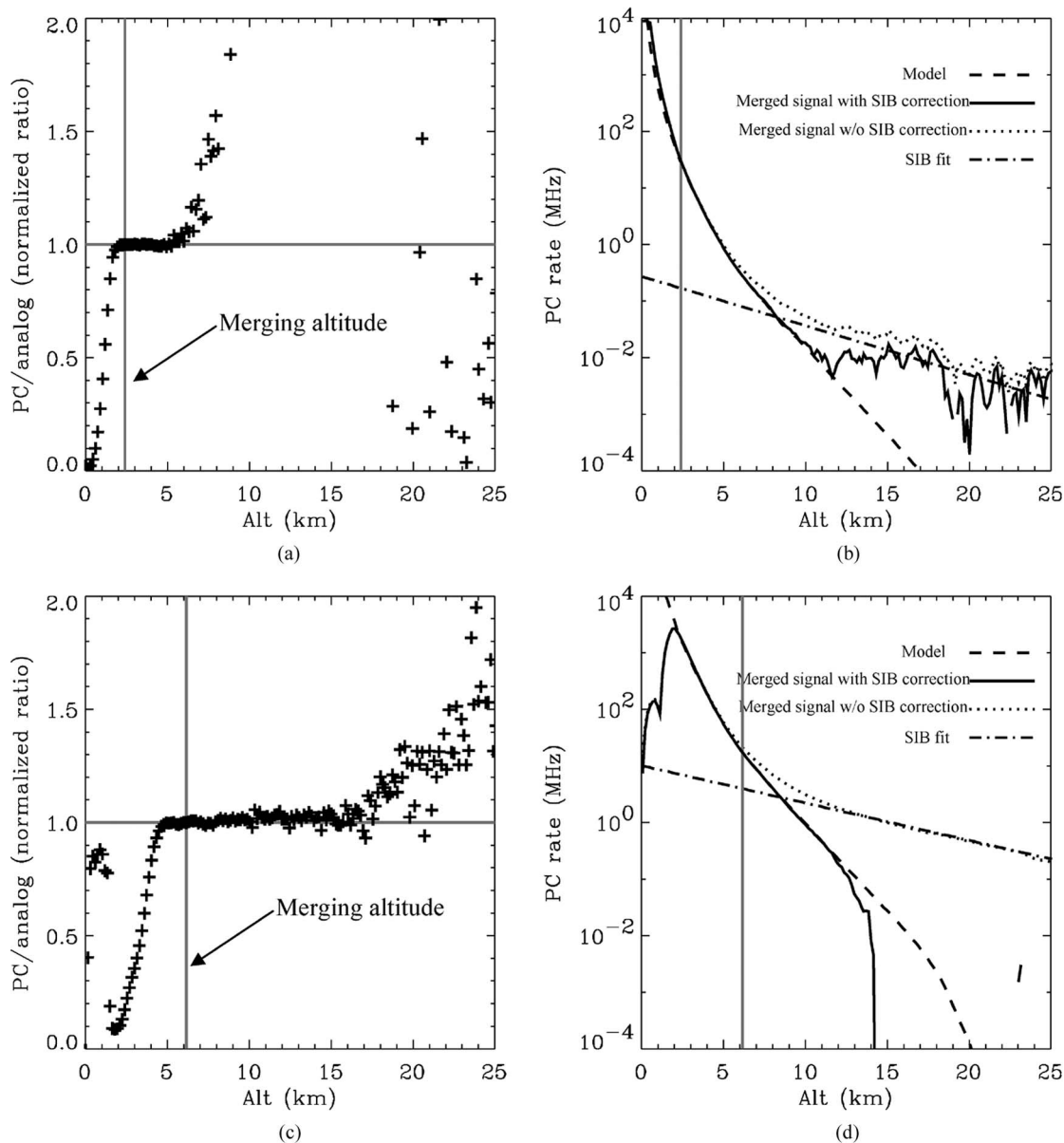


Fig. 3. Examples of signal merging and SIB correction for the 285-nm signal. The 10-min averaged data occurred at 13:00 local time on October 18, 2008. (a) Normalized ratio of PC to analog after background and dead-time corrections for the low-altitude channel signal. (b) Comparison of the non-SIB-corrected signal, the SIB-corrected signal, and the model, as well as the SIB fitting function, for the low-altitude signal. The model uses the coincident ozonesonde measurement assuming no aerosol. The SIB fitting function ( $\exp(-1.3 - alt \cdot 2 \cdot 10^{-1})$ ) was empirically derived using previously retrieved data and coincident ozonesonde measurements. (c) Same as (a) but for the high-altitude channel. (d) Same as (b) but for the high-altitude channel. The coefficients of the SIB fitting function result from an empirical single-exponential least squares fit to the signal acquired from 100 to 160  $\mu$ s after data acquisition starts.

squares fit to data acquired approximately from 100 to 160  $\mu$ s after data acquisition starts where the SIB becomes dominant. The start and length of the exponential fit vary with different channels (either wavelength channels or altitude channels), atmospheric structures, and lidar configurations because these parameters affect the intensity of the detected signal. For our low-altitude channel, the SIB is weaker than that of the high-altitude channel because of the different PMT and weaker signal. However, it is difficult to automatically determine the fitting function for the low-altitude channel signal using the least squares fitting method, particularly for the 285-nm signal, because the far-range signal after background correction is not completely characterized by an exponential function

[Fig. 3(b)]. It is useful to optimize the exponential fitting function for the low-altitude channel using previous retrieval data and compare the data with coincident ozonesonde profiles. The slope of the logarithm of the SIB fitting function remains for a particular configuration (i.e., outgoing power) and could slightly change for different configurations. Those retrievals corrected using the empirically derived exponential function agree with ozonesonde profiles up to 5 km within 5% bias. Fig. 3 shows the typical effect of the SIB correction and the comparison of the fully corrected signal and the model for the 285-nm signal. The model simulation employs the coincident ozonesonde measurement assuming no aerosol.

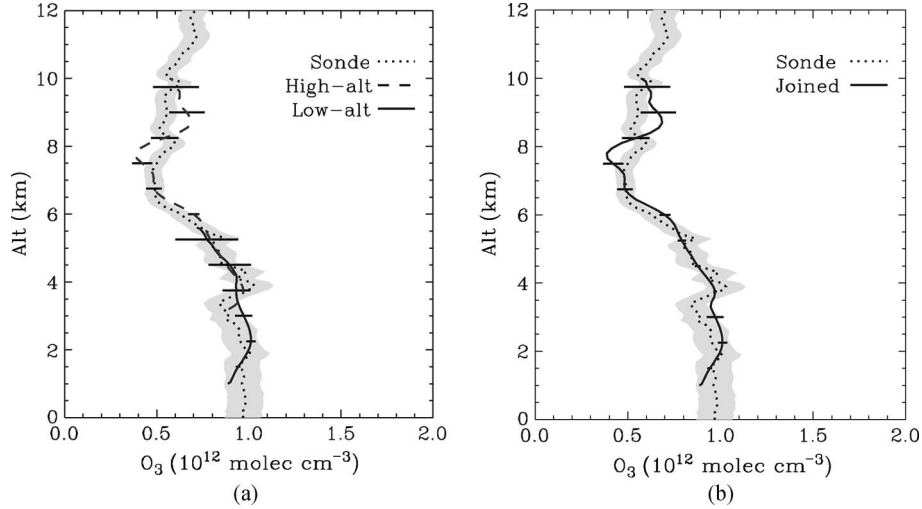


Fig. 4. Example of a joined ozone retrieval for the lidar data in Fig. 3. (a) Separate retrievals of the two altitude channels. The error bars represent the one-sigma statistical uncertainties. The gray envelope represents  $\pm 10\%$  uncertainty of the coincident ozonesonde profile. (b) Joined DIAL retrieval from the two altitude channels and its combined one-sigma statistical uncertainty.

### B. DIAL Retrieval

Excellent discussions concerning the DIAL technique occur in the publications by Measures [63], Kovalev and Eichinger [64], and Browell *et al.* [39]. The average ozone number density  $n_{(r+\Delta r/2)}$  between range  $r$  and  $r + \Delta r$  can be expressed as the summation of the signal term  $n_{(r+\Delta r/2)}^s$ , the differential backscattering term  $\Delta n_{(r+\Delta r/2)}^b$ , and the differential extinction term  $\Delta n_{(r+\Delta r/2)}^e$

$$n_{(r+\Delta r/2)} = n_{(r+\Delta r/2)}^s + \Delta n_{(r+\Delta r/2)}^b + \Delta n_{(r+\Delta r/2)}^e. \quad (2)$$

One can write the discrete forms of the three terms at the right side as follows:

$$n_{(r+\Delta r/2)}^s = \frac{1}{2\Delta r \Delta \sigma_{O_3}} \ln \left( \frac{P_{\text{on}}(r) P_{\text{off}}(r+\Delta r)}{P_{\text{off}}(r) P_{\text{on}}(r+\Delta r)} \right) \quad (3)$$

$$\Delta n_{(r+\Delta r/2)}^b = -\frac{1}{2\Delta r \Delta \sigma_{O_3}} \ln \left( \frac{\beta_{\text{on}}(r) \beta_{\text{off}}(r+\Delta r)}{\beta_{\text{off}}(r) \beta_{\text{on}}(r+\Delta r)} \right) \quad (4)$$

$$\Delta n_{(r+\Delta r/2)}^e = -\frac{1}{\Delta \sigma_{O_3}} (\alpha_{\text{on}}(r+\Delta r/2) - \alpha_{\text{off}}(r+\Delta r/2)) \quad (5)$$

where the subscripts “on” and “off” represent the online (285 nm) and offline (291 nm) wavelengths, respectively,  $P$  is the detected photon counts,  $\beta$  is the total backscatter coefficient,  $\alpha$  is the total extinction coefficient excluding ozone, and  $\Delta \sigma_{O_3}$  is the differential ozone absorption cross section.  $P$ ,  $\beta$ , and  $\alpha$  are dependent on  $r$  and the wavelength. Strictly speaking,  $\Delta \sigma_{O_3}$  is  $r$  dependent as well because it is a function of temperature, which varies with  $r$ . By ignoring the differential scattering and extinction from non-ozone species, the DIAL equation reduces to only  $n^s$ .  $\Delta n^b$  arises from aerosol differential backscattering.  $\Delta n^e$  consists of differential Rayleigh extinction, aerosol extinction, and non-ozone gaseous absorption, including  $O_2$ ,  $SO_2$ , and  $NO_2$ . Measurements from a meteorological sounding can usually correct Rayleigh effects. We correct the aerosol effects when they are significantly enough, particularly in PBL. The aerosol correction discussion appears in Section III-D.

### C. Joining Retrievals From Two Adjacent Altitude Channels

Final retrievals result from joining the data from two altitude channels with a weighted average. We choose to join the final ozone retrievals instead of the raw signals because the SNRs of the two altitude channels at the joining altitude are significantly different. If the retrievals derived from two different channels are statistically independent, the best estimate of these measurements is the two-channel weighted average [65]

$$n_{\text{best}} = \frac{\sum_{i=1}^2 w_i n_i}{\sum_{i=1}^2 w_i} \quad (6)$$

where  $n_i$  is the ozone retrieval of channel  $i$  and the weight  $w_i$  is the inverse square of the corresponding statistical uncertainty ( $\varepsilon_{1i}$ , which will be discussed in Section V)

$$w_i = 1/\varepsilon_{1i}^2. \quad (7)$$

The uncertainty of  $n_{\text{best}}$  is

$$\varepsilon_{1\text{best}} = \left( \sum_{i=1}^2 w_i \right)^{-1/2}. \quad (8)$$

Typically, the low- and high-altitude channels join between 3.3 and 4.4 km. Fig. 4 shows an example of a joined ozone profile, as well as the combined one-sigma statistical uncertainties.

### D. Aerosol Correction

In a polluted area, aerosols can be a dominant error source in the lower troposphere. Based on (4) and (5), the vertical gradient of aerosol backscattering determines  $\Delta n^b$ , and the magnitude of the differential aerosol extinction coefficient determines  $\Delta n^e$ . The largest aerosol correction usually occurs in an inhomogeneous aerosol layer (i.e., the top of the PBL). One can solve for the ozone and aerosol profiles simultaneously with only two wavelengths by assuming appropriate Ångström

exponents and constant lidar ratios [66], [67]. If a third wavelength is available and is close to the DIAL wavelength pair, one can use the dual-DIAL technique [68], [69] to reduce the error due to aerosol. When the third wavelength is far from the DIAL wavelength pair, one can use the method suggested by Browell *et al.* [39] to correct the aerosol interference. Without the third wavelength, we employ an iterative procedure to retrieve ozone and correct aerosol effects. To illustrate this method, start with the equation for ozone number density using only the 291-nm signal [63]

$$n_{(r+\Delta r/2)} = \frac{1}{2\sigma_{O_3}\Delta r} \times \left\{ \ln\left(\frac{P(r)}{P(r+\Delta r)}\right) - \ln\left[\frac{(\beta_{(r)}^M + \beta_{(r)}^A)/r^2}{(\beta_{(r+\Delta r)}^M + \beta_{(r+\Delta r)}^A)/(r+\Delta r)^2}\right] - 2\left(\alpha_{(r+\Delta r/2)}^M + \alpha_{(r+\Delta r/2)}^A\right)\Delta r \right\} \quad (9)$$

where  $\sigma_{O_3}$  is the ozone absorption cross section,  $\beta_{(r)}^M$  and  $\beta_{(r)}^A$  are the molecular and aerosol backscatter coefficients at range  $r$ , respectively, and  $\alpha_{(r+\Delta r/2)}^M$  and  $\alpha_{(r+\Delta r/2)}^A$  represent the average molecular and aerosol extinction coefficients, respectively, between range  $r$  and  $r + \Delta r$ . The subscript 291 is omitted for brevity because all backscatter and extinction parameters correspond to 291 nm. Solving for  $\beta_{(r)}^A$ , (9) becomes

$$\beta_{(r)}^A = \exp\left\{ \ln\left(\frac{P(r)}{P(r+\Delta r)}\right) - 2n_{(r+\Delta r/2)}\sigma_{O_3}\Delta r - 2\left(\alpha_{(r+\Delta r/2)}^M + \alpha_{(r+\Delta r/2)}^A\right)\Delta r \right\} \times \frac{r^2\left(\beta_{(r+\Delta r)}^M + \beta_{(r+\Delta r)}^A\right)}{(r+\Delta r)^2} - \beta_{(r)}^M. \quad (10)$$

Assuming that the lidar ratio (aerosol extinction-to-backscatter ratio), i.e.,  $S = \alpha^A/\beta^A$ , is known for the 291-nm signal and further assuming that

$$\alpha_{(r+\Delta r/2)}^A \approx \alpha_{(r+\Delta r)}^A = S\beta_{(r+\Delta r)}^A \quad (11)$$

(10) only contains the following two unknown variables: the aerosol backscatter coefficient  $\beta_{(r+\Delta r)}^A$  and the ozone number density  $n_{(r+\Delta r/2)}$ . Molecular backscatter and extinction can be computed from nearby radiosonde data or from climatology. For the first iteration step,  $n_{(r+\Delta r/2)}$  can be computed from (3) and inserted into (10). By assuming a start value  $\beta_{(ref)}^A$  at a reference range and a constant  $S$  with range,  $\beta_{(r)}^A$  can be solved by (10). Then, the first  $\beta_{(r)}^A$  profile is substituted back into (10) to compute the second estimate by using a more accurate form for  $\alpha_{(r+\Delta r/2)}^A$  as

$$\alpha_{(r+\Delta r/2)}^A = S\left(\beta_{(r+\Delta r)}^A + \beta_{(r)}^A\right)/2 \quad (12)$$

where  $\beta_{(r)}^{A'}$  represents the value from the first estimate. With several iterations of (10) and (12) (we name this iteration the ‘‘aerosol iteration’’), we can get a stable solution for  $\beta_{(r)}^A$ , which does not change significantly from one iteration step to the next. The aerosol iteration stop criterion is defined as  $\xi_{(l)}^A < \xi_{min}^A$ .  $\xi_{(l)}^A$  is the relative total difference of the backscatter coefficients between two adjacent iteration steps and is defined as

$$\xi_{(l)}^A = \frac{1}{\sum_{r=r_s}^{r_{ref}} \beta_{(r,l)}^A} \sum_{r=r_s}^{r_{ref}} \left| \beta_{(r,l)}^A - \beta_{(r,l+1)}^A \right| \quad (13)$$

where  $l$  represents the iteration step,  $r_s$  is the starting range of the lidar retrieval, and  $\beta_{(r,l)}^A$  are the backscatter coefficients at range  $r$  and iteration step  $l$ .  $\xi_{min}^A$  is typically 0.01 for our aerosol retrievals. Aside from  $\xi_{min}^A$ , the number of iterations required for a stable solution is also related to the range resolution of the signal. For simplicity, we assume that the power-law dependences with wavelength for the aerosol extinction and backscatter coefficients are the same although they can be different theoretically.  $\Delta n_{(r+\Delta r)}^b$  and  $\Delta n_{(r+\Delta r)}^e$  can be approximated as [39]

$$\Delta n_{(r+\Delta r)}^b \approx \frac{(4-\eta)\Delta\lambda}{2\Delta r\Delta\sigma_{O_3}\lambda_{off}} \left( \frac{B(r)}{1+B(r)} - \frac{B(r+\Delta r)}{1+B(r+\Delta r)} \right) \quad (14)$$

$$\Delta n_{(r+\Delta r)}^e \approx -\frac{\Delta\lambda}{\Delta\sigma_{O_3}\lambda_{off}} \left( \eta\alpha_{(r+\Delta r/2)}^A + 4\alpha_{(r+\Delta r/2)}^M \right) \quad (15)$$

where  $\eta$  is the Ångström exponent,  $\Delta\lambda$  is the wavelength separation, and  $B_{(r)}$  is the aerosol-to-molecular backscatter ratio at the offline wavelength defined as

$$B_{(r)} = \beta_{(r)}^A/\beta_{(r)}^M. \quad (16)$$

The estimate for the aerosol-corrected ozone number density profile is then substituted into (10) to calculate an updated aerosol backscatter profile, which, in turn, is used to compute an updated aerosol-corrected ozone profile. This iteration is named ‘‘ozone iteration’’ to be distinct with the coupled aerosol iteration process. A similar iteration stop criterion,  $\xi_{(l)}^{O_3} < \xi_{min}^{O_3}$ , as the aerosol iteration, can be defined for the ozone iteration by replacing the backscatter coefficient in (13) with the ozone number density. Typically, only two ozone iterations are required when  $\xi_{min}^{O_3}$  is set equal to 0.001.

The lidar ratio ( $S$ ) exhibits a wide range of variation with different aerosol refractive indexes, size distributions, and humidity [70]. The  $S$  measurements have been made most frequently at 308 [71] and 355 nm [72], [73]. The  $S$  for our DIAL wavelengths was assumed to be  $60 \text{ sr}^{-1}$  [74] constant over the measurement range for typical urban aerosols. The Ångström exponent ( $\eta$ ) is often seen as an indicator of aerosol particle size: Values greater than two correspond to small smoke particles, and values smaller than one correspond to large particles like sea salt [75], [76]. Most of the reported  $\eta$ 's for tropospheric aerosol are measured at wavelengths longer than 300 nm with a variation from zero to two [77], [78]. Considering that  $\eta$  could be relatively small when it is applied in the UV region,

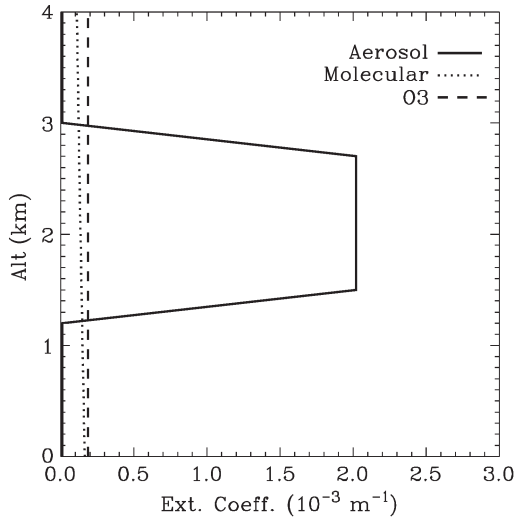


Fig. 5. Aerosol, molecular, and ozone extinction coefficient profiles at 291 nm for a model calculation of extreme aerosol effects.

we assume that  $\eta = 0.5$  at our DIAL wavelengths for urban aerosols [79].

Simulations were conducted to investigate the aerosol correction in the DIAL retrieval under an extremely large aerosol gradient condition by assuming the aerosol, molecular, and ozone extinction profiles at 291 nm shown in Fig. 5. The hypothetical aerosol profile includes the following three basic regimes: homogeneous, increasing, and decreasing extinction. The aerosol extinction coefficients are set equal to  $10^{-5} \text{ m}^{-1}$  below 1.2 km and above 3 km to represent a background value. The resulting steep gradient between the low background and high aerosol value provides an extreme test for the aerosol correction algorithm. The molecular extinction profile is derived from the 1976 U.S. Standard Atmosphere [80]. The assumed ozone extinction profile is constant with altitude and is based on a number density of  $1.5 \times 10^{12} \text{ molec} \cdot \text{cm}^{-3}$  and an absorption cross section of  $1.24 \times 10^{-18} \text{ cm}^2 \cdot \text{molec}^{-1}$  at 291 nm [81].

Fig. 6 shows the comparison of the ozone retrieval both with and without aerosol correction, as well as the calculated aerosol profile, at 291 nm. This example calculation assumes that  $\eta = 0.5$  and  $S = 60 \text{ sr}^{-1}$  are known exactly, and there is no signal measurement error. With a range resolution of 150 m, two ozone iterations produce the final aerosol-corrected ozone retrieval by setting  $\xi_{\text{min}}^{O_3} = 0.001$ . In the process of calculating the aerosol profile, aerosol iterations produce a stable aerosol solution by setting  $\xi_{\text{min}}^A = 0.01$ , which is approximately identical to the model aerosol profile. The aerosol correction procedure reduces the retrieval errors from  $\pm 50\%$  to about  $\pm 5\%$ . The residual errors are due to the numerical integration and the approximation of (14) and (15). The quality of this iterative procedure depends on the choice of  $S$  and  $\eta$ . According to (10), (14) and (15),  $S$  affects the aerosol profile retrieval, while  $\eta$  affects only the final ozone correction.

Fig. 7 shows the sensitivity test for  $S$  and  $\eta$  in the aerosol correction assuming that  $S = 60$  and  $\eta = 0.5$  are the correct values. Inaccurate estimates of  $S$  or  $\eta$  can yield retrieval errors up to about 20%. Larger  $\eta$  will overestimate  $\Delta n^e$ , which produces less ozone, and vice versa.  $\eta$  has a smaller impact

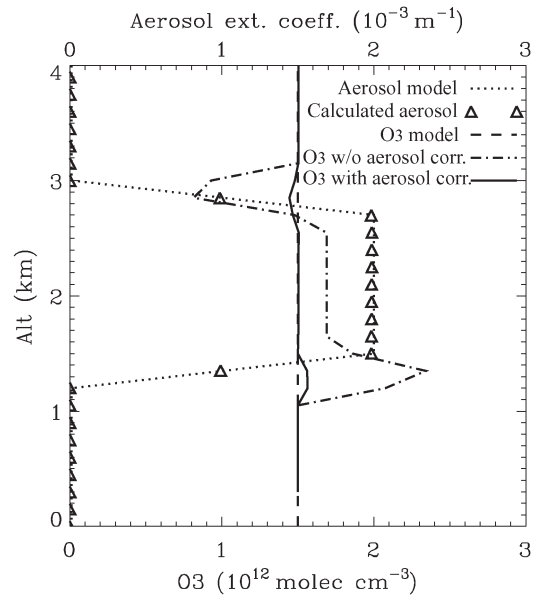


Fig. 6. Comparison of the simulated ozone retrieval without aerosol correction against that with aerosol correction using the iterative procedure. The Ångström exponent ( $\eta$ ) and lidar ratio ( $S$ ) were assumed to be exactly known at  $0.5$  and  $60 \text{ sr}^{-1}$ , respectively, for the aerosol correction. The aerosol correction dramatically improves the ozone retrieval.

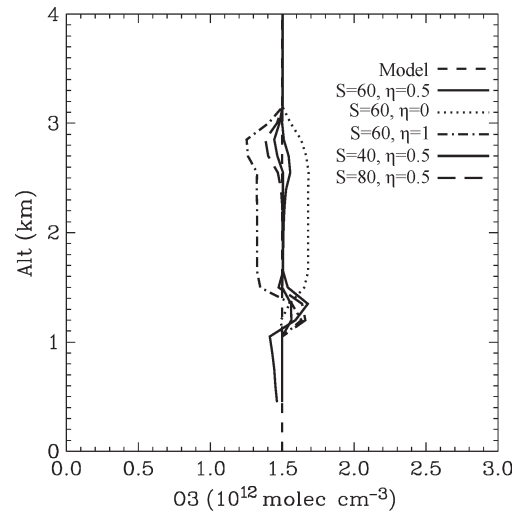


Fig. 7. Ozone retrieval using different Ångström exponents ( $\eta = 0, 0.5$ , and  $1$ ) and lidar ratios ( $S = 40, 60$ , and  $80$ ) in the aerosol correction.

on  $\Delta n^b$  relative to  $\Delta n^e$  due to the  $4 - \eta$  factor. The impact of  $S$  is larger in the inhomogeneous aerosol layer than in the homogeneous layer. The peak error is larger for underestimated  $S$  relative to overestimated  $S$  [82].

We summarize the iterative procedure as follows.

- 1) Calculate the first estimate of the ozone concentration from (3).
- 2) Substitute the first estimated ozone into (10) to derive the aerosol backscatter profile for the offline wavelength, and iterate to obtain a stable solution with (12).
- 3) Calculate the differential aerosol backscatter and extinction corrections to obtain a second estimate of ozone using (14) and (15).
- 4) With the second ozone estimate, go back to step 2.



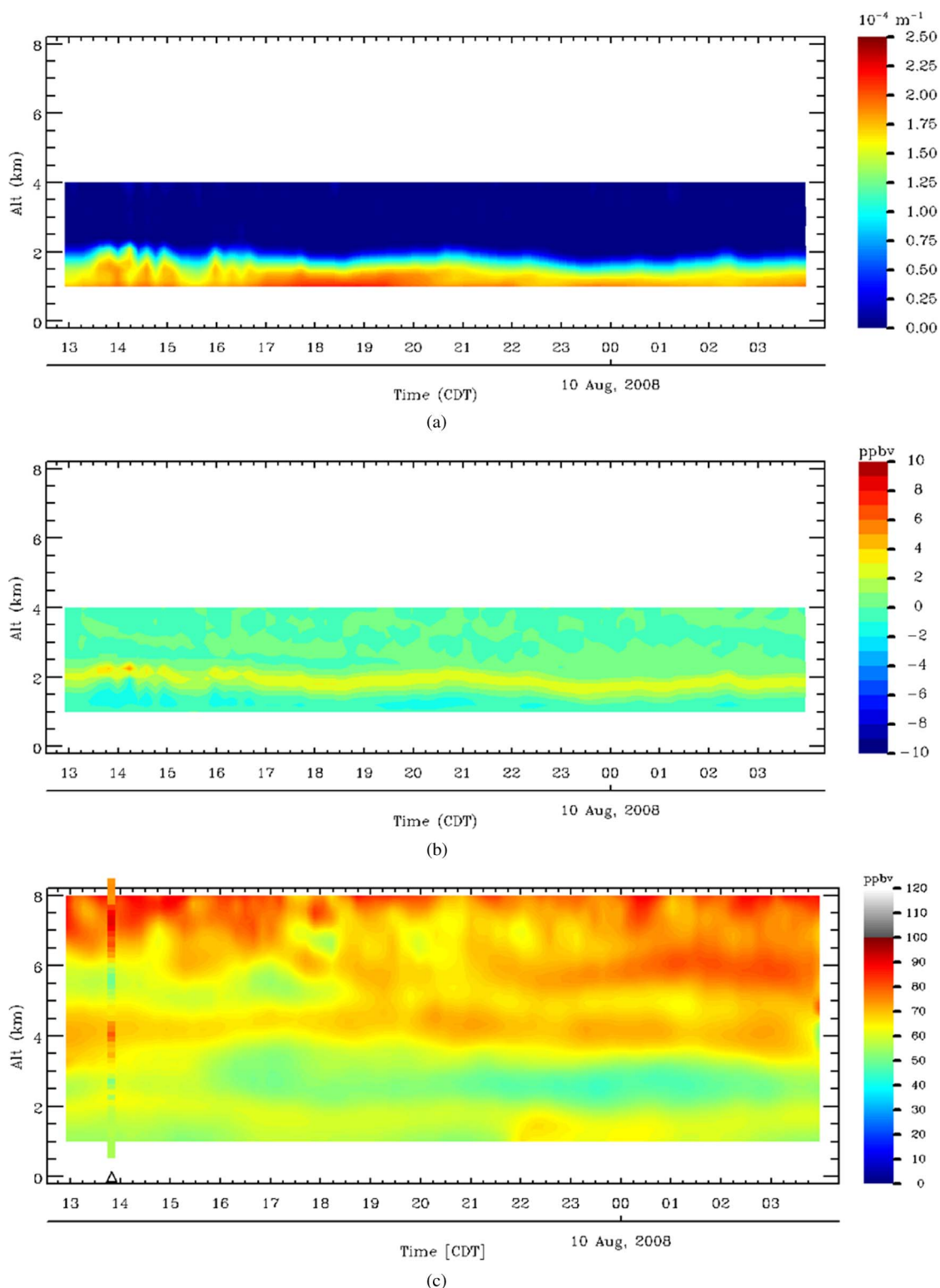


Fig. 8. Ozone DIAL retrievals made on August 9–10, 2008. (a) Calculated aerosol extinction coefficient at 291 nm. (b) Aerosol correction for ozone DIAL retrieval. (c) Ozone DIAL retrieval after aerosol correction. The retrieval was made with a 750-m vertical range resolution and a 10-min temporal resolution. The colocated ozonesonde marked by a triangle was launched at 13:49 local time.

#### IV. MEASUREMENTS

Fig. 8 shows an ozone DIAL retrieval for 15 consecutive hours from 12:56 local time, August 9, to 03:56, August 10, 2008, with 10-min temporal integration (12 000 shots) and

750-m vertical range resolution using the data processing described in the previous section. The aerosol correction was made only at altitudes between 1 and 4 km using the data from the low-altitude channel because of the negligible aerosol effects above 4 km. The aerosol time–height curtain [Fig. 8(a)]

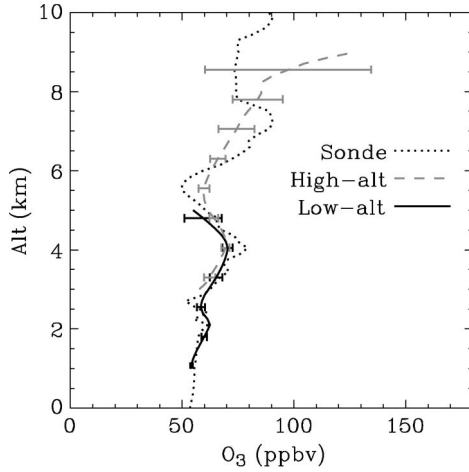


Fig. 9. Mean ozone mixing ratio and one-sigma standard deviation for the 10-min vertical profiles between 12:56 and 15:06 local time in Fig. 8. The colocated ozonesonde was launched at 13:49 local time. The large error bar ( $\sim 45\%$ ) at 8.5 km identifies the high-altitude limit of the retrievals (8 km).

exhibits moderate aerosol activity below 2 km with expected diurnal PBL variation and shorter timescale fluctuations due to PBL processes. The maximum aerosol correction in Fig. 8(b) corresponds to an ozone adjustment of 3–4 ppbv and occurs between 1.5 and 2.5 km for the largest vertical backscatter gradient. The retrievals for the two altitude channels overlap between 3.3 and 4.4 km to produce the final ozone profiles [Fig. 8(c)] that agree well with the colocated ozonesonde (EN-SCI model 2Z with unbuffered 2% cathode solution) launched at 13:49 local time. The time–height curtain of ozone’s evolution shows a very interesting structure of multiple ozone layers in the lower atmosphere that varies with time. One can see the buildup and decay of various layers throughout this 12-h period. The high-frequency variation in the high-altitude channel ( $\geq 6$  km) results partly from lower SNR and higher uncertainty of the SIB correction, both of which increase with altitude. Fig. 9 shows the mean ozone profile and one-sigma standard deviation for the 10-min vertical profiles between 12:56 and 15:06 local time in Fig. 8, as well as the coincident ozonesonde measurement. The high-altitude channel has a standard deviation increasing with altitude due to the statistical error distribution. Its standard deviation is less than 13 ppbv below 8 km and increases to about 45 ppbv at 8.5 km where the 285-nm laser does not have sufficient SNR for ozone retrieval; therefore, we terminate the retrievals at 8 km in Fig. 8. The standard deviation of the low-altitude channel retrievals is less than 5 ppbv below 4 km and reaches 8 ppbv at 5 km due to lower SNR. The standard deviation at 2 km is a little larger than the surrounding altitudes possibly because of larger ozone fluctuations or larger uncertainties of the aerosol correction in the ozone retrieval at the PBL top. The two altitude channels have consistent mean retrievals in the overlap region with discrepancies less than 5 ppbv and similar standard deviations at 3.3 km which most likely reflect the true ozone short-term variations above the PBL as shown in Fig. 8. The mean retrievals agree with the ozonesonde measurement within about 10 ppbv and have higher biases at the upper altitudes.

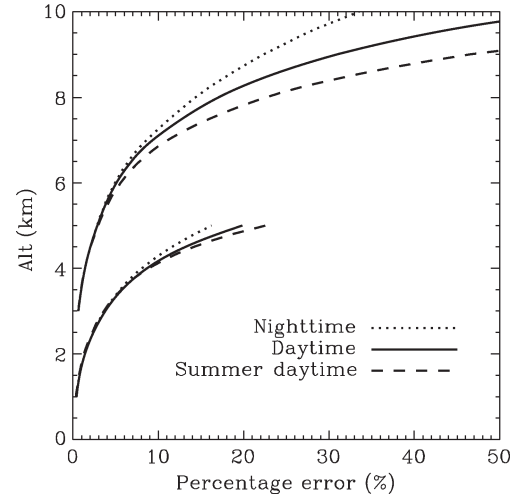


Fig. 10. Estimated statistical errors for the high- and low-altitude channels using 10-min integration and 750-m range resolution. The nighttime and daytime statistical errors are modeled by using the annually averaged local ozonesonde profile, the 1976 U.S. Standard Atmosphere, an urban aerosol model [83], and the lidar parameters in Table I. The ozone profile used for summer daytime errors is assumed 20% higher than the annual average.

## V. ERROR ANALYSIS

We divide the error budget of the DIAL retrieval into the following four categories: 1) statistical uncertainties  $\varepsilon_1$  arising from signal and background noise fluctuations; 2) errors  $\varepsilon_2$  associated with differential backscatter and extinction of non-ozone gases ( $O_2$ ,  $SO_2$ ,  $NO_2$ , etc.) and aerosols; 3) errors  $\varepsilon_3$  due to uncertainties in the ozone absorption cross section; and 4) errors  $\varepsilon_4$  related to instrumentation and electronics.  $\varepsilon_1$  is a random error;  $\varepsilon_2$ ,  $\varepsilon_3$ , and  $\varepsilon_4$  are systematic errors.  $\varepsilon_1$  can be written as [41]

$$\varepsilon_1 = \frac{1}{2n\Delta r\Delta\sigma_{O_3}} \sqrt{\sum_{j,\lambda} \frac{1}{(SNR_{j,\lambda})^2}}. \quad (17)$$

With the assumption of a Poisson distribution governing PC, the SNR at wavelength  $\lambda$  and range registration  $j$  becomes

$$SNR_{j,\lambda} = \frac{P_{j,\lambda}}{(P_{j,\lambda} + P_b + P_d)^{1/2}} \quad (18)$$

where  $P_b$  is the solar background counts and  $P_d$  is the dark counts. It is straightforward to show that  $\varepsilon_1$  is proportional to  $(\Delta r^3 N A P_L)^{-1/2}$ , where  $N$  represents the total number of shots,  $A$  is the unobscured area of the telescope’s primary mirror, and  $P_L$  is the number of emitted laser photons.  $\Delta r$  must be chosen large enough to produce an acceptably small error. Fig. 10 shows the estimated statistical errors for the high- and low-altitude channels for a 10-min integration and a 750-m range resolution.  $\varepsilon_1$  is typically less than 10% below 4 km for our low-altitude channel and could be 20% at 5 km. This altitude performance gives us sufficient overlap for the two altitude channels under most atmospheric conditions. In the high-altitude channel,  $\varepsilon_1$  exceeds 25% of the retrieval ozone near  $8 \pm 1$  km, where we terminate the retrieval.

$\varepsilon_2$  includes the interference from  $O_2$ ,  $SO_2$ ,  $NO_2$ , air molecules, and aerosols. Table II summarizes the potential errors

TABLE II  
DIAL RETRIEVAL ERRORS DUE TO NON-OZONE ABSORPTION GASES

Gases	$\Delta\sigma$ , differential absorption cross-section ( $\text{cm}^2 \text{molec}^{-1}$ ) for 285 and 291 nm	References for $\Delta\sigma$	Mixing ratio (ppbv)	References for mixing ratio	O <sub>3</sub> retrieval error (%)
O <sub>3</sub>	$1.15 \times 10^{-18}$	Bass and Paur 1981 [84]	60		
O <sub>2</sub> <sup>a</sup>	$4.5 \times 10^{-27}$	Fally <i>et al.</i> 2000 [85]	$2.1 \times 10^8$		1.5%
SO <sub>2</sub>	$-4.8 \times 10^{-20}$	Rufus <i>et al.</i> 2003 [86]	13 <sup>b</sup>	NREM 2006 [88]	-0.9%
NO <sub>2</sub>	$-2.25 \times 10^{-20}$	Bogumil <i>et al.</i> 2003 [87]	18 <sup>c</sup>	NREM 2006 [88]	-0.6%
Total					$\pm 1.5\%$

<sup>a</sup> due to O<sub>2</sub>-O<sub>2</sub>

<sup>b</sup> maximum 24-hr average in 1994. Latest local monitoring data available.

<sup>c</sup> Annual arithmetic average in 1993. Latest local monitoring data available.

TABLE III  
SUMMARY OF THE ERRORS IN RAPCD OZONE DIAL MEASUREMENTS

Errors	Low-altitude channel (1-4 km)	High-altitude channel (3-8 km)
1. $\epsilon_1$ , statistical error	<10%	<25%
2. $\epsilon_2$ , interference by non-ozone species		
Aerosol	<20%	<5 %
Non-ozone absorption gases		<1.5%
Rayleigh	<1% using local radiosonde profile	
3. $\epsilon_3$ , due to uncertainty in $\Delta\sigma_{O_3}$		<3%
4. $\epsilon_4$ , due to SIB and dead-time	<5%	<10%
Total RMS error	<23%	<28%

\* The errors are estimated by assuming a 60 ppbv constant ozone mixing ratio in the troposphere for data with a 750-m vertical resolution and 10-min integration.

in the DIAL retrieval for 285- and 291-nm wavelengths due to non-ozone absorption gases [84]–[88]. The calculation of the oxygen dimer (O<sub>2</sub>–O<sub>2</sub>) interference includes some uncertainties due to the absorption cross-sectional measurement. The O<sub>2</sub>–O<sub>2</sub> absorption theory has not been entirely established [89]. Local SO<sub>2</sub> and NO<sub>2</sub> profiling data are not available. However, the estimated error due to either SO<sub>2</sub> or NO<sub>2</sub> using the latest ground observation is less than 1%. The impact caused by differential Rayleigh extinction results in an inaccuracy of less than 1% using balloon ozonesonde retrievals of atmospheric density or by employing climatological models.

The main concern comes from the aerosol interference, which depends on both the wavelengths and wavelength separation. Although the aerosol optical properties could be retrieved from a third wavelength, the differential effect for a DIAL wavelength pair still has some uncertainty due to the assumption for lidar ratio and Ångström exponent. Within the PBL, where the statistical errors are small, differential aerosol backscattering and extinction dominate the error sources [39], [41], [43]. However, it is reasonable to believe that the error

due to aerosol interference is smaller than 20% after the aerosol correction, as shown in Section III-D.

The uncertainty in the Bass–Paur ozone cross sections is believed to be less than 2% [81], [84], [89].  $\epsilon_3$  will be less than 3% after considering the temperature dependence.

$\epsilon_4$  could be caused by a misalignment of the lasers with the telescope FOV, imperfect dead time, or SIB correction. Dead time distorts the near-range signal, and SIB distorts the far-range signal. Because the dead-time behavior is reliably characterized, the error caused by SIB usually is larger than the dead-time error. These errors related to the signal non-linearity can be experimentally diagnosed by a function-generator-driven LED laser simulator [90], [91]. For the 10-min integration data,  $\epsilon_4$  is estimated to be < 5% at 1–4 km for our low-altitude channel and < 10% for our high-altitude channel below 8 km based on our LED test results and the analysis of our previous data such as Figs. 8 and 9. A summary of the errors in the DIAL measurements is shown in Table III for a constant tropospheric ozone of 60 ppbv, 750-m vertical resolution, and 10-min integration.

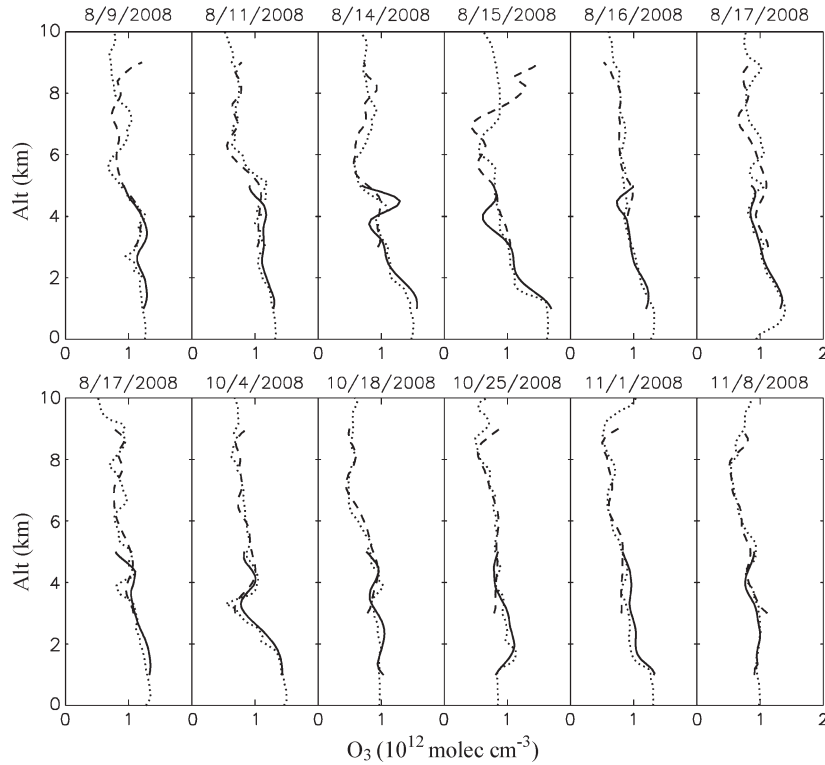


Fig. 11. Comparison of (solid line) low- and (dashed line) high-altitude-channel aerosol-corrected retrievals with the (dotted line) coincident ozonesonde measurements.

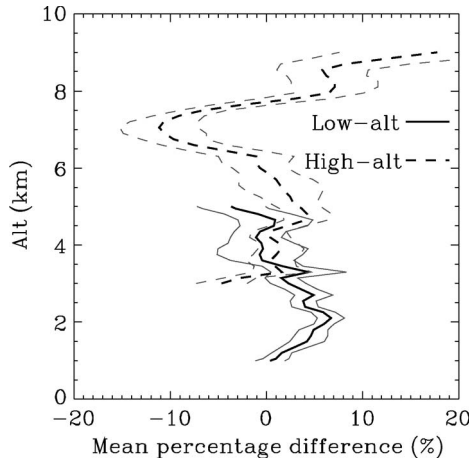


Fig. 12. (Dark) Mean percentage differences, lidar sonde/sonde, and (gray) their estimated one-sigma standard error of the mean for the data in Fig. 11.

Fig. 11 shows a comparison of 12 lidar retrievals and their single coincident ozonesonde measurement between 13:00 and 14:00 local time except for the first profile on August 17, 2008 (upper right panel), which was taken at 08:00. The aerosol correction was made at altitudes between 1 and 4 km by setting the reference altitude at  $\sim 6$  km and  $\beta_{(\text{ref})}^A = 1.67 \times 10^{-7} \text{ m}^{-1} \cdot \text{sr}^{-1}$  [83]. Fig. 12 shows the mean percentage differences and their standard errors of the mean for all those retrievals. The lidar retrievals of the low-altitude channel agree with ozonesonde measurements within 10% from 1 to 4 km. The relatively high errors at about 2 km possibly relate to residual aerosol correction errors around PBL height. The lidar retrievals from

the high-altitude channel agree with ozonesonde to within 20% below 8 km. The statistical error and the uncertainty associated with the SIB correction result in larger errors for the high-altitude channel above 6 km.

## VI. CONCLUSION AND FUTURE PLANS

The RAPCD ozone DIAL system measures tropospheric ozone profiles during both daytime and nighttime using the 285-/291-nm wavelength pair. The low-altitude receiving channel makes ozone measurements at altitudes between 1 and 5 km using a 10-cm telescope and Hamamatsu R7400U PMTs. The high-altitude channel measures ozone between 3 and about 8 km using a 40-cm telescope and EMI 9813 PMTs. Model calculations demonstrate that the iterative aerosol correction procedure significantly reduces the retrieval error arising from differential aerosol backscatter in the lower troposphere where the quality of the aerosol correction depends on the accuracy of the *a priori* lidar ratio and Ångström exponent. A comparison of the lidar retrievals and coincident ozonesonde measurements suggests that retrieval accuracy ranges from better than 10% after the application of an aerosol correction below 4 km to better than 20% for altitudes below 8 km with 750-m vertical resolution and 10-min integration. Error sources include statistical uncertainty, differential scattering and absorption from non-ozone species, uncertainty in ozone absorption cross section, and imperfection of the dead-time and SIB corrections. The uncertainty in the SIB correction and the statistical errors dominate the error sources in the free troposphere and could be reduced by increasing the integration time or reducing the range resolution.

Future improvements will overcome two major limitations of the current system by doing the following: 1) extending observations into the upper troposphere by replacing the current transmitters with more powerful ones and shifting the current wavelengths to longer ones to make higher-altitude nighttime measurements and 2) minimizing aerosol interference in the lower troposphere by adding a third wavelength (dual-DIAL technique). This lidar with expected improvements will provide a unique data set to investigate the chemical and dynamical processes in the PBL and free troposphere. The spatiotemporal variance estimates derived from the ozone lidar observations will also be useful for assessing the variance of tropospheric ozone captured by satellite retrievals.

#### ACKNOWLEDGMENT

The authors would like to thank T. McGee, S. McDerimid, and T. Leblanc for the extensive discussions, J. Kaye, P. K. Bhartia, and R. McPeters for the continuing support, and the UAHuntsville ozonesonde team, namely, R. Williams, P. Buckley, and D. Nuding, for providing the ozonesonde data. The authors would also like to thank W. Guerin for editing the manuscript.

#### REFERENCES

- [1] D. Jacob, *Introduction to Atmospheric Chemistry*. Princeton, NJ: Princeton Univ. Press, 1999.
- [2] D. Shindell, G. Faluvegi, A. Lacis, J. Hansen, R. Ruedy, and E. Aguilar, "Role of tropospheric ozone increases in 20th-century climate change," *J. Geophys. Res.*, vol. 111, no. D8, p. D08 302, Apr. 2006.
- [3] J. Lelieveld and F. J. Dentener, "What controls tropospheric ozone?" *J. Geophys. Res.*, vol. 105, no. D3, pp. 3531–3551, Feb. 2000.
- [4] J. Stutz, B. Alicke, R. Ackermann, A. Geyer, A. White, and E. Williams, "Vertical profiles of NO<sub>3</sub>, N<sub>2</sub>O<sub>5</sub>, O<sub>3</sub>, and NO<sub>x</sub> in the nocturnal boundary layer: 1. Observations during the Texas Air Quality Study 2000," *J. Geophys. Res.*, vol. 109, no. D12, p. D12 306, Jun. 2004.
- [5] A. Geyer and J. Stutz, "Vertical profiles of NO<sub>3</sub>, N<sub>2</sub>O<sub>5</sub>, O<sub>3</sub>, and NO<sub>x</sub> in the nocturnal boundary layer: 2. Model studies on the altitude dependence of composition and chemistry," *J. Geophys. Res.*, vol. 109, no. D12, p. D12 307, Jun. 2004.
- [6] J. Liang, L. W. Horowitz, D. J. Jacob, Y. Wang, A. M. Fiore, J. A. Logan, G. M. Gardner, and J. W. Munger, "Seasonal budgets of reactive nitrogen species and ozone over the United States, and export fluxes to the global atmosphere," *J. Geophys. Res.*, vol. 103, no. D11, pp. 13 435–13 450, Jun. 1998.
- [7] W. B. Grant, E. V. Browell, C. F. Butler, M. A. Fenn, M. B. Clyton, J. R. Hannan, H. E. Fuelberg, D. R. Blake, N. J. Blake, G. L. Gregory, B. G. Heikes, G. W. Sachse, H. B. Singh, J. Snow, and R. W. Talbot, "A case study of transport of tropical marine boundary layer and lower tropospheric air masses to the northern midlatitude upper troposphere," *J. Geophys. Res.*, vol. 105, no. D3, pp. 3757–3769, Feb. 2000.
- [8] H. Eisele, H. E. Scheel, R. Sladkovic, and T. Trickl, "High-resolution lidar measurements of stratosphere–troposphere exchange," *J. Atmos. Sci.*, vol. 56, no. 2, pp. 319–330, Jan. 1999.
- [9] A. Stohl, P. Bonasoni, P. Cristofanelli, W. Collins, J. Feichter, A. Frank, C. Forster, E. Gerasopoulos, H. Gäggeler, P. James, T. Kentarchos, H. Kromp-Kolb, B. Krüger, C. Land, J. Meloan, A. Papayannis, A. Priller, P. Seibert, M. Sprenger, G. J. Roelofs, H. E. Scheel, C. Schnabel, P. Siegmund, L. Tobler, T. Trickl, H. Wernli, V. Wirth, P. Zanis, and C. Zerefos, "Stratosphere–troposphere exchange: A review and what we learned from STACCATO," *J. Geophys. Res.*, vol. 108, no. D12, p. 8516, 2003.
- [10] A. O. Langford, C. D. Masters, M. H. Proffitt, E.-Y. Hsie, and A. F. Tuck, "Ozone measurements in a tropopause fold associated with a cut-off low system," *Geophys. Res. Lett.*, vol. 23, no. 18, pp. 2501–2504, 1996.
- [11] A. J. DeCaria, K. E. Pickering, G. L. Stenchikov, and L. E. Ott, "Lightning-generated NO<sub>x</sub> and its impact on tropospheric ozone production: A three-dimensional modeling study of a stratosphere–troposphere experiment: Radiation, aerosols and ozone (STERAO-A) thunderstorm," *J. Geophys. Res.*, vol. 110, no. D14, p. D14 303, Jul. 2005.
- [12] O. R. Cooper, A. Stohl, M. Trainer, A. M. Thompson, J. C. Witte, S. J. Oltmans, G. Morris, K. E. Pickering, J. H. Crawford, G. Chen, R. C. Cohen, T. H. Bertram, P. Wooldridge, A. Perring, W. H. Brune, J. Merrill, J. L. Moody, D. Tarasick, P. Nédélec, G. Forbes, M. J. Newchurch, F. J. Schmidlin, B. J. Johnson, S. Turquet, S. L. Baughcum, X. Ren, F. C. Fehsenfeld, J. F. Meagher, N. Spichtinger, C. C. Brown, S. A. McKeen, I. S. McDerimid, and T. Leblanc, "Large upper tropospheric ozone enhancements above midlatitude North America during summer: *In situ* evidence from the IONS and MOZAIC ozone measurement network," *J. Geophys. Res.*, vol. 111, no. D24, p. D24 S05, Dec. 2006.
- [13] O. R. Cooper, M. Trainer, A. M. Thompson, S. J. Oltmans, D. W. Tarasick, J. C. Witte, A. Stohl, S. Eckhardt, J. Lelieveld, M. J. Newchurch, B. J. Johnson, R. W. Portmann, L. Kalnajs, M. K. Dube, T. Leblanc, I. S. McDerimid, G. Forbes, D. Wolfe, T. Carey-Smith, G. A. Morris, B. Lefer, B. Rappenglück, E. Joseph, F. Schmidlin, J. Meagher, F. C. Fehsenfeld, T. J. Keating, R. A. V. Curen, and K. Minschwaner, "Evidence for a recurring eastern North America upper tropospheric ozone maximum during summer," *J. Geophys. Res.*, vol. 112, no. D23, p. D23 304, Dec. 2007.
- [14] U. Schumann and H. Huntrieser, "The global lightning-induced nitrogen oxides source," *Atmos. Chem. Phys.*, vol. 7, no. 14, pp. 3823–3907, 2007.
- [15] S. J. Oltmans, H. Levy, II, J. M. Harris, J. T. Merrill, J. L. Moody, J. A. Lathrop, E. Cuevas, M. Trainer, M. S. O'Neill, J. M. Prospero, H. Vömel, and B. J. Johnson, "Summer and spring ozone profiles over the North Atlantic from ozonesonde measurements," *J. Geophys. Res.*, vol. 101, no. D22, pp. 29 179–29 200, Dec. 1996.
- [16] M. J. Newchurch, M. A. Ayoub, S. Oltmans, B. Johnson, and F. J. Schmidlin, "Vertical distribution of ozone at four sites in the United States," *J. Geophys. Res.*, vol. 108, no. D1, p. 4031, Jan. 15, 2003.
- [17] R. D. McPeters, G. J. Labow, and B. J. Johnson, "A satellite-derived ozone climatology for balloonsonde estimation of total column ozone," *J. Geophys. Res.*, vol. 102, no. D7, pp. 8875–8885, Apr. 1997.
- [18] J. P. Burrows, M. Weber, M. Buchwitz, V. Rozanov, A. Ladstätter-Weienmayer, A. Richter, R. DeBeek, R. Hoogen, K. Bramstedt, K.-U. Eichmann, and M. Eisinger, "The Global Ozone Monitoring Experiment (GOME): mission concept and first scientific results," *J. Atmos. Sci.*, vol. 56, no. 2, pp. 151–175, Jan. 1999.
- [19] M. J. Newchurch, D. M. Cunnold, and J. Cao, "Intercomparison of Stratospheric Aerosol and Gas Experiment (SAGE) with Umkehr [64] and Umkehr [92] ozone profiles and time series: 1979–1991," *J. Geophys. Res.*, vol. 103, no. D23, pp. 31 277–31 292, Dec. 1998.
- [20] M. J. Newchurch, E. S. Yang, D. M. Cunnold, G. C. Reinsel, J. M. Zawodny, and J. M. Russell, III, "Evidence for slowdown in stratospheric ozone loss: First stage of ozone recovery," *J. Geophys. Res.*, vol. 108, no. D16, p. 4507, Aug. 23, 2003.
- [21] J. M. Russell, III, L. L. Gordley, J. H. Park, S. R. Drayson, W. D. Hesketh, R. J. Cicerone, A. F. Tuck, J. E. Frederick, J. E. Harries, and P. J. Crutzen, "The halogen occultation experiment," *J. Geophys. Res.*, vol. 98, no. D6, pp. 10 777–10 797, Jun. 1993.
- [22] J. W. Waters, L. Froidevaux, G. L. Manney, W. G. Read, and L. S. Elson, "MLS observations of lower stratospheric ClO and O<sub>3</sub> in the 1992 southern hemisphere winter," *Geophys. Res. Lett.*, vol. 20, no. 12, pp. 1219–1222, Jun. 1993.
- [23] X. Liu, K. Chance, C. E. Sioris, R. J. D. Spurr, T. P. Kurosu, R. V. Martin, and M. J. Newchurch, "Ozone profile and tropospheric ozone retrievals from global ozone monitoring experiment: Algorithm description and validation," *J. Geophys. Res.*, vol. 110, no. D20, p. D20 307, Oct. 2005.
- [24] J. R. Ziemke, S. Chandra, B. N. Duncan, L. Froidevaux, P. K. Bhartia, P. F. Levelt, and J. W. Waters, "Tropospheric ozone determined from Aura OMI and MLS: Evaluation of measurements and comparison with the global modeling initiative's chemical transport model," *J. Geophys. Res.*, vol. 111, no. D19, p. D19 303, Oct. 2006.
- [25] Y. Choi, Y. Wang, T. Zeng, D. Cunnold, E.-S. Yang, R. Martin, K. Chance, V. Thouret, and E. Edgerton, "Springtime transitions of NO<sub>2</sub>, CO, and O<sub>3</sub> over North America: Model evaluation and analysis," *J. Geophys. Res.*, vol. 113, no. D20, p. D20 311, Oct. 2008.
- [26] Q. Yang, D. M. Cunnold, H.-J. Wang, L. Froidevaux, H. Claude, J. Merrill, M. Newchurch, and S. J. Oltmans, "Midlatitude tropospheric ozone columns derived from the Aura Ozone monitoring instrument and microwave limb sounder measurements," *J. Geophys. Res.*, vol. 112, no. D20, p. D20 305, Oct. 2007, DOI:10.1029/2007JD008528.
- [27] J. H. Kim, M. J. Newchurch, and K. Han, "Distribution of tropical tropospheric ozone determined by the scan-angle method applied to TOMS measurements," *J. Atmos. Sci.*, vol. 58, no. 18, pp. 2699–2708, Sep. 2001.

- [28] J. H. Kim and M. J. Newchurch, "Biomass-burning influence on tropospheric ozone over New Guinea and South America," *J. Geophys. Res.*, vol. 103, no. D1, pp. 1455–1461, Jan. 1998.
- [29] J. H. Kim, S. Na, M. J. Newchurch, and R. V. Martin, "Tropical tropospheric ozone morphology and seasonality seen in satellite and *in situ* measurements and model calculations," *J. Geophys. Res.*, vol. 110, no. D2, p. D02 303, Jan. 2005.
- [30] X. Liu, K. Chance, C. E. Sioris, T. P. Kurosu, R. Spurr, R. V. Martin, T. Fu, J. Logan, D. Jacob, P. Palmer, M. J. Newchurch, I. A. Megretskaya, and R. B. Chatfield, "First directly retrieved global distribution of tropospheric column ozone from GOME: Comparison with the GEOS-CHEM model," *J. Geophys. Res.*, vol. 111, no. D2, p. D02 308, Jan. 2006.
- [31] X. Liu, K. Chance, C. E. Sioris, T. P. Kurosu, and M. J. Newchurch, "Intercomparison of GOME, ozonesonde, and SAGE II measurements of ozone: Demonstration of the need to homogenize available ozonesonde data sets," *J. Geophys. Res.*, vol. 111, no. D14, p. D14 305, Jul. 2006.
- [32] R. Beer, "TES on the Aura mission: Scientific objectives, measurements, and analysis overview," *IEEE Trans. Geosci. Remote Sens.*, vol. 44, no. 5, pp. 1102–1105, May 2006.
- [33] P. F. Levelt, E. Hilsenrath, G. W. Leppelmeier, G. H. J. van den Oord, P. K. Bhartia, J. Tamminen, J. F. de Haan, and J. P. Veefkind, "Science objectives of the ozone monitoring instrument," *IEEE Trans. Geosci. Remote Sens.*, vol. 44, no. 5, pp. 1199–1208, May 2006.
- [34] W. Steinbrecht, T. J. McGee, L. W. Twigg, H. Claude, F. Schönborn, G. K. Sumnicht, and D. Silbert, "Intercomparison of stratospheric ozone and temperature profiles during the October 2005 Hohenpeißenberg Ozone Profiling Experiment (HOPE)," *Atmos. Meas. Tech.*, vol. 2, no. 1, pp. 125–145, 2009.
- [35] T. Trickl, N. Bärtsch-Ritter, H. Eisele, M. Furger, R. Mücke, and A. Stöhl, "High-ozone layers in the middle and upper troposphere above Central Europe: Strong import from the stratosphere over the Pacific Ocean," *Atmos. Chem. Phys. Discuss.*, vol. 9, no. 1, pp. 3113–3166, Jan. 2009.
- [36] Y. Zhao, R. D. Marchbanks, and R. M. Hardesty, "ETL's transportable lower troposphere ozone lidar and its applications in air quality studies," *Proc. SPIE*, vol. 3127, pp. 53–62, 1997.
- [37] R. J. Alvarez, II, W. A. Brewer, D. C. Law, J. L. Machol, R. D. Marchbanks, S. P. Sandberg, C. J. Senff, and A. M. Weickmann, "Development and application of the TOPAZ airborne lidar system by the NOAA Earth System Research Laboratory," in *Proc. 24th Int. Laser Radar Conf.*, 2008, pp. 68–71.
- [38] G. Ancellet, A. Papayannis, J. Pelon, and G. Mégie, "DIAL tropospheric ozone measurement using a Nd:YAG laser and the Raman shifting technique," *J. Atmos. Ocean. Technol.*, vol. 6, no. 5, pp. 832–839, Oct. 1989.
- [39] E. V. Browell, S. Ismail, and S. T. Shipley, "Ultraviolet DIAL measurements of O<sub>3</sub> profiles in regions of spatially inhomogeneous aerosols," *Appl. Opt.*, vol. 24, no. 17, pp. 2827–2836, Sep. 1985.
- [40] T. Fukuchi, T. Fujii, N. Cao, and K. Nemoto, "Tropospheric O<sub>3</sub> measurements by simultaneous differential absorption lidar and null profiling," *Opt. Eng.*, vol. 40, no. 9, pp. 1944–1949, Sep. 2001.
- [41] A. Papayannis, G. Ancellet, J. Pelon, and G. Mégie, "Multi-wavelength lidar for ozone measurements in the troposphere and the lower stratosphere," *Appl. Opt.*, vol. 29, no. 4, pp. 467–476, Feb. 1990.
- [42] M. H. Proffitt and A. O. Langford, "Ground-based differential absorption lidar system for day or night measurements of ozone throughout the free troposphere," *Appl. Opt.*, vol. 36, no. 12, pp. 2568–2585, Apr. 1997.
- [43] J. A. Sunesson, A. Apituley, and D. P. J. Swart, "Differential absorption lidar system for routine monitoring of tropospheric ozone," *Appl. Opt.*, vol. 33, no. 30, pp. 7045–7058, Oct. 1994.
- [44] J. L. Machol, R. D. Marchbanks, C. J. Senff, B. J. McCarty, W. L. Eberhard, W. A. Brewer, R. A. Richter, R. J. Alvarez, II, D. C. Law, A. M. Weickmann, and S. P. Sandberg, "Scanning tropospheric ozone and aerosol lidar with double-gated photomultipliers," *Appl. Opt.*, vol. 48, no. 3, pp. 512–524, Jan. 2009.
- [45] I. S. McDermid, D. A. Haner, M. M. Kleiman, T. D. Walsh, and M. L. White, "Differential absorption lidar system for tropospheric and stratospheric ozone measurements," *Opt. Eng.*, vol. 30, no. 1, pp. 22–30, Jan. 1991.
- [46] T. J. McGee, M. R. Gross, U. N. Singh, J. J. Butler, and P. E. Kimvilakani, "Improved stratospheric ozone lidar," *Opt. Eng.*, vol. 34, no. 5, pp. 1421–1430, May 1995.
- [47] J. Pelon, S. Godin, and G. Mégie, "Upper stratospheric (30–50 km) lidar observations of the ozone vertical distribution," *J. Geophys. Res.*, vol. 91, no. D8, pp. 8667–8671, 1986.
- [48] O. Uchino and I. Tabata, "Mobile lidar for simultaneous measurements of ozone, aerosols, and temperature in the stratosphere," *Appl. Opt.*, vol. 30, no. 15, pp. 2005–2012, May 1991.
- [49] E. V. Browell, S. Ismail, and W. B. Grant, "Differential absorption lidar (DIAL) measurements from air and space," *Appl. Phys. B, Photophys. Laser Chem.*, vol. 67, no. 4, pp. 399–410, Oct. 1998.
- [50] O. R. Cooper, A. Stöhl, S. Eckhardt, D. D. Parrish, S. J. Oltmans, B. J. Johnson, P. Nédélec, F. J. Schmidlin, M. J. Newchurch, Y. Kondo, and K. Kita, "A springtime comparison of tropospheric ozone and transport pathways on the east and west coasts of the United States," *J. Geophys. Res.*, vol. 110, no. D5, p. D05 S90, Mar. 2005.
- [51] G. J. Megie, G. Ancellet, and J. Pelon, "Lidar measurements of ozone vertical profiles," *Appl. Opt.*, vol. 24, no. 21, pp. 3454–3463, Nov. 1985.
- [52] A. E. Siegman, Standard for the Measurement of Beam Widths, Beam Divergence, and Propagation Factors, Proposal for a Working Draft: ISO1991.
- [53] J. Burris, W. Heaps, B. Gary, W. Hoegy, L. Lait, T. McGee, M. Gross, and U. Singh, "Lidar temperature measurements during the Tropical Ozone Transport Experiment (TOTE)/Vortex Ozone Transport Experiment (VOTE) mission," *J. Geophys. Res.*, vol. 103, no. D3, pp. 3505–3510, 1998.
- [54] J. Burris, T. McGee, W. Hoegy, P. Newman, L. Lait, L. Twigg, G. Sumnicht, W. Heaps, C. Hostetler, R. Neuber, and K. F. Künzi, "Lidar temperature measurements during the SOLVE campaign and the absence of polar stratospheric clouds from regions of very cold air," *J. Geophys. Res.*, vol. 107, no. D20, p. 8297, Oct. 2002.
- [55] D. P. Donovan, J. A. Whiteway, and A. I. Carswell, "Correction for nonlinear photon-counting effects in lidar systems," *Appl. Opt.*, vol. 32, no. 33, pp. 6742–6753, Nov. 1993.
- [56] M. Lampton and J. Bixler, "Counting efficiency of systems having both paralyzable and nonparalyzable elements," *Rev. Sci. Instrum.*, vol. 56, no. 1, pp. 164–165, Jan. 1985.
- [57] D. N. Whiteman, B. Demoz, P. D. Girolamo, J. Comer, I. Veselovskii, K. Evans, Z. Wang, M. Cadirola, K. Rush, G. Schwemmer, B. Gentry, S. H. Melfi, B. Mielke, D. Venable, and T. V. Hove, "Raman lidar measurements during the International H<sub>2</sub>O Project. Part I: Instrumentation and analysis techniques," *J. Atmos. Ocean. Technol.*, vol. 23, no. 2, pp. 157–169, Feb. 2006.
- [58] R. K. Newsom, D. D. Turner, B. Mielke, M. Clayton, R. Ferrare, and C. Sivaraman, "Simultaneous analog and photon counting detection for Raman lidar," *Appl. Opt.*, vol. 48, no. 20, pp. 3903–3914, Jul. 2009.
- [59] Photomultiplier Handbook, Burle, Lancaster, PA, 1989.
- [60] F. Cairo, F. Congeduti, M. Poli, S. Centurioni, and G. D. Donfrancesco, "A survey of the signal-induced noise in photomultiplier detection of wide dynamics luminous signals," *Rev. Sci. Instrum.*, vol. 67, no. 9, pp. 3274–3280, Sep. 1996.
- [61] Y. Zhao, "Signal-induced fluorescence in photomultipliers in differential absorption lidar systems," *Appl. Opt.*, vol. 38, no. 21, pp. 4639–4648, Jul. 1999.
- [62] T. J. McGee, R. A. Ferrare, D. N. Whiteman, J. J. Butler, J. F. Burris, and M. A. Owens, "Lidar measurements of stratospheric ozone during the STOIC campaign," *J. Geophys. Res.*, vol. 100, no. D5, pp. 9255–9262, 1995.
- [63] M. R. Measures, *Laser Remote Sensing: Fundamentals and Applications*. New York: Wiley, 1984.
- [64] V. A. Kovalev and W. E. Eichinger, *Elastic Lidar Theory, Practice, and Analysis Methods*. New York: Wiley, 2004.
- [65] J. R. Taylor, *An Introduction to Error Analysis: The Study of Uncertainties in Physical Measurements*. Mill Valley, CA: Oxford Univ. Press, 1982.
- [66] F. Immler, "A new algorithm for simultaneous ozone and aerosol retrieval from tropospheric DIAL measurements," *Appl. Phys. B, Photophys. Laser Chem.*, vol. 76, no. 5, pp. 593–596, May 2003.
- [67] Y. Sasano, "Simultaneous determination of aerosol and gas distribution by DIAL measurements," *Appl. Opt.*, vol. 27, no. 13, pp. 2640–2641, Jul. 1988.
- [68] V. A. Kovalev and M. P. Bristow, "Compensational three-wavelength differential-absorption lidar technique for reducing the influence of differential scattering on ozone-concentration measurements," *Appl. Opt.*, vol. 35, no. 24, pp. 4790–4797, Aug. 1996.
- [69] Z. Wang, H. Nakane, H. Hu, and J. Zhou, "Three-wavelength dual differential absorption lidar method for stratospheric ozone measurements in the presence of volcanic aerosols," *Appl. Opt.*, vol. 36, no. 6, pp. 1245–1252, Feb. 1997.
- [70] R. Pedros, V. Estelles, M. Sicard, J. L. Gomez-Amo, M. P. Utrillas, J. A. Martinez-Lozano, F. Rocadenbosch, C. Perez, and J. M. B. Recio, "Climatology of the aerosol extinction-to-backscatter

ratio from sun-photometric measurements,” *IEEE Trans. Geosci. Remote Sens.*, vol. 48, no. 1, pp. 237–249, Jan. 2010.

[71] A. Ansmann, M. Riebesell, U. Wandinger, C. Weitkamp, W. E. Voss, W. Lahmann, and W. Michaelis, “Combined Raman elastic-backscatter LIDAR for vertical profiling of moisture, aerosol extinction, backscatter, and LIDAR ratio,” *Appl. Phys. B, Photophys. Laser Chem.*, vol. 55, no. 1, pp. 18–28, Jul. 1992.

[72] R. Ferrare, S. Melfi, D. Whiteman, K. Evans, and R. Leifer, “Raman lidar measurements of aerosol extinction and backscattering 1. Methods and comparisons,” *J. Geophys. Res.*, vol. 103, no. D16, pp. 19663–19672, 1998.

[73] D. Müller, A. Ansmann, I. Mattis, M. Tesche, U. Wandinger, D. Althausen, and G. Pisani, “Aerosol-type-dependent lidar ratios observed with Raman lidar,” *J. Geophys. Res.*, vol. 112, no. D16, p. D16202, Aug. 2007.

[74] J. Ackermann, “The extinction-to-backscatter ratio of tropospheric aerosol: A numerical study,” *J. Atmos. Ocean. Technol.*, vol. 15, no. 4, pp. 1043–1050, Aug. 1998.

[75] D. Westphal and O. Toon, “Simulations of microphysical, radiative, and dynamical processes in a continental scale forest fire smoke plume,” *J. Geophys. Res.*, vol. 96, no. D12, pp. 22379–22400, 1991.

[76] G. L. Schuster, O. Dubovik, and B. N. Holben, “Ångström exponent and bimodal aerosol size distributions,” *J. Geophys. Res.*, vol. 111, no. D7, pp. D07207.1–D07207.14, Apr. 2006.

[77] C. M. Carrico, M. H. Bergin, J. Xu, K. Baumann, and H. Maring, “Urban aerosol radiative properties: Measurements during the 1999 Atlanta Supersite experiment,” *J. Geophys. Res.*, vol. 108, no. D7, p. 8422, Feb. 2003.

[78] D. Müller, I. Mattis, U. Wandinger, A. Ansmann, D. Althausen, and A. Stohl, “Raman lidar observations of aged Siberian and Canadian forest fire smoke in the free troposphere over Germany in 2003: Microphysical particle characterization,” *J. Geophys. Res.*, vol. 110, no. D17, p. D17201, Sep. 2005.

[79] T. F. Eck, B. N. Holben, J. S. Reid, O. Dubovik, A. Smirnov, N. T. O’Neill, I. Slutsker, and S. Kinne, “Wavelength dependence of the optical depth of biomass burning, urban, and desert dust aerosols,” *J. Geophys. Res.*, vol. 104, no. D24, pp. 31333–31349, Dec. 27, 1999.

[80] NOAA, U.S. Standard Atmosphere, Washington, DC: Government Printing Office, 1976.

[81] J. Orphal and K. Chance, “Ultraviolet and visible absorption cross-sections for HITRAN,” *J. Quant. Spectrosc. Radiat. Transf.*, vol. 82, no. 1–4, pp. 491–504, Nov./Dec. 2003.

[82] V. A. Kovalev, “Sensitivity of the lidar solution to errors of the aerosol backscatter-to-extinction ratio: Influence of a monotonic change in the aerosol extinction coefficient,” *Appl. Opt.*, vol. 34, no. 18, pp. 3457–3462, Jun. 1995.

[83] A. S. Jursa, *Handbook of Geophysics and the Space Environment*. Hanscom AFB, MA: Air Force Geophys. Lab., 1985.

[84] A. M. Bass and R. J. Paur, “Absorption cross-sections for ozone: The temperature dependence,” *J. Photochem.*, vol. 17, p. 141, 1981.

[85] S. Fally, A. C. Vandaele, M. Carleer, C. Hermans, A. Jenouvrier, M.-F. Mérienne, B. Coquart, and R. Colin, “Fourier transform spectroscopy of the O<sub>2</sub> Herzberg bands. III. Absorption cross-sections of the collision-induced bands and of the Herzberg continuum,” *J. Mol. Spectrosc.*, vol. 204, no. 1, pp. 10–20, Nov. 2000.

[86] J. Rufus, G. Stark, P. L. Smith, J. C. Pickering, and A. P. Thorne, “High-resolution photoabsorption cross section measurements of SO<sub>2</sub>, 2: 220 to 325 nm at 295 K,” *J. Geophys. Res.*, vol. 108, no. E2, p. 5011, Feb. 2003.

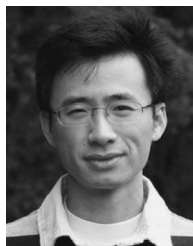
[87] K. Bogumil, J. Orphal, T. Homann, S. Voigt, P. Spietz, O. C. Fleischmann, A. Vogel, M. Hartmann, H. Bovensmann, J. Frerick, and J. P. Burrows, “Measurements of molecular absorption spectra with the SCIAMACHY pre-flight model: Instrument characterization and reference data for atmospheric remote-sensing in the 230–2380 nm region,” *J. Photochem. Photobiol. A, Chem.*, vol. 157, no. 2/3, pp. 167–184, May 2003.

[88] Air Quality Report, Data Summaries, Trend Analysis and Program Activities (2001–2005), Natural Resources Environ. Manage. Division, Huntsville, AL, 2006.

[89] J. Orphal, “A critical review of the absorption cross-sections of O<sub>3</sub> and NO<sub>2</sub> in the 240–790 nm region,” *J. Photochem. Photobiol. A*, vol. 157, no. 2/3, pp. 185–209, May 2003.

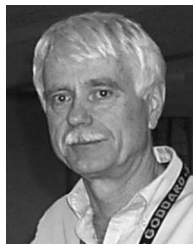
[90] M. P. Bristow, D. H. Bundy, and A. G. Wright, “Signal linearity, gain stability, and gating in photomultipliers: Application to differential absorption lidars,” *Appl. Opt.*, vol. 34, no. 21, pp. 4437–4452, Jul. 1995.

[91] H. S. Lee, G. K. Schwemmer, C. L. Corb, M. Dombrowski, and C. Prasad, “Gated photomultiplier response characterization for DIAL measurements,” *Appl. Opt.*, vol. 29, no. 22, pp. 3303–3315, Aug. 1, 1990.



**Shi Kuang** received the M.Sc. degree in electrical engineering and the Ph.D. degree in atmospheric science from The University of Alabama in Huntsville (UAHuntsville), Huntsville, in 2009.

He is currently with the Earth System Science Center, Atmospheric Science Department, UAHuntsville. His current fields of interest include lidar remote sensing, tropospheric ozone, and air quality study.



**John F. Burris** received the Ph.D. degree in physics from the University of Maryland, College Park.

He is currently a Lidar Scientist with the NASA Goddard Space Flight Center, Greenbelt, MD, where he has been employed for 30 years. The focus of his work involves developing lidar systems to measure ozone, temperature, CO<sub>2</sub>, and CH<sub>4</sub> remotely on Earth and Mars.



**M. J. Newchurch** received the B.Sc. degree in industrial sciences from Colorado State University, Fort Collins, in 1974 and the Ph.D. degree in atmospheric sciences from the Georgia Institute of Technology, Atlanta, in 1986.

Since 1988, he has been with the Atmospheric Science Department, The University of Alabama in Huntsville (UAHuntsville), Huntsville, where he is currently a Professor. He conceived, designed, built, and currently directs the Regional Atmospheric Profiling Center for Discovery laboratory and the UAHuntsville/National Oceanic and Atmospheric Administration Ozone sonde station. His current fields of interest include tropospheric ozone profile measurements with lidars and ozonesondes, retrievals from satellite instruments, atmospheric photochemical modeling, and ozone trend analyses.



**Steve Johnson** received the B.S.E.E. degree from Purdue University, West Lafayette, IN, in 1977 and the M.S.E.E. degree from The University of Alabama in Huntsville, Huntsville, in 1987.

He is currently with the Earth Science Office, NASA Marshall Space Flight Center, Huntsville, where he has worked on the development and application of lidars and radiometers for profiling of winds and atmospheric constituents.



**Stephanie Long** received the B.Sc. degree in physics from The University of Alabama in Huntsville (UAHuntsville), Huntsville, in 2010.

Since 2007, she has been with the Atmospheric Chemistry Group, Earth System Science Center, Huntsville. Her responsibilities include the Huntsville Differential Absorption Lidar system, as well as managing the Huntsville Ozone sonde Station.